



Observed surface wave variations in the background current field of the Kuroshio Extension

Hongxuan Wu^{1,2} · Jingkai Li^{1,2} · Zhaohui Chen^{1,2} · Xin Ma^{1,2}

Received: 4 July 2024 / Accepted: 16 December 2024
© Springer-Verlag GmbH Germany, part of Springer Nature 2024

Abstract

Ocean wave-current interactions are important physical processes at the sea surface, which can potentially cause extreme sea states under certain conditions. Usually, such interactions are more notable in regions with strong waves and background currents. In this study, focusing on the Kuroshio Extension, we used buoy-measured and altimeter-derived wave data to determine variations in wave properties with the background currents. Statistically, the wave height can be underestimated (overestimated) by approximately 4% (3%) when the current and waves are in the opposite (same) direction. In regions with warm (cold) eddies, the wave height and wavelength inside the eddy are larger (smaller) than those outside by approximately 5% and 8% (4% and 4%), respectively, and the wave direction is deflected by 11° anticlockwise (clockwise). The wavenumber spectra of wave height and surface current speed are highly correlated with a power law of k^{-2} – k^{-3} at scales of 20–200 km for swell-dominated cases. Additionally, the convergence and divergence of wave energy resulting from the current-induced refraction of swell are captured. From another perspective, the wave-induced Stokes drift calculated using the directional spectrum accounts for 54% of the reanalysis surface currents, and the accuracy of the estimated surface current can be improved by up to 14% by considering Stokes drift. This study provided quantitative analysis of observed surface wave variations in the Kuroshio Extension region from multiple perspectives.

Keywords Surface wave observations · Kuroshio extension · Wave-current interactions · Mesoscale eddy · Stokes drift

1 Introduction

As an indicator of the sea state, sea surface waves have direct influence not only on the physical processes at the air-sea interface and in the upper ocean, but also on maritime

navigation and other ocean-based human activities. Many studies have been conducted to improve the understanding and modeling of ocean waves, e.g., to help forecast extreme wave events with higher accuracy. Although sea surface winds dominate the generation of ocean surface waves, background currents might also modulate waves during their propagation, and vice versa.

In early work, Longuet-Higgins and Stewart (1962) identified that waves and currents were coupled by wave-induced radiation stress, and that nonlinear interactions between them would affect both the wave amplitude and the current velocity. In the following decades, wave-current interactions have been widely distinguished through various types of field observations. In the presence of surface ocean currents, wave frequency might experience Doppler shift (Tolman 1991; Villas Bôas et al. 2020) that leads to change in the propagation speed, and the regulation of wave height can cause altered steepness and possibly wave breaking (Peregrine 1976). As Cheng et al. (2022) and Wang et al. (2020) showed, the wave height would increase (decrease) when waves run in the opposite (same) direction

Responsible Editor Yasumasa Miyazawa

✉ Jingkai Li
ljkl1105@ouc.edu.cn
Hongxuan Wu
whx2226@stu.ouc.edu.cn
Zhaohui Chen
chenzhaohui@ouc.edu.cn
Xin Ma
maxin@ouc.edu.cn

¹ Physical Oceanography Laboratory/Institute for Advanced Ocean Science/Frontiers Science Center for Deep Ocean Multispheres and Earth System, Ocean University of China, Qingdao, China

² Laoshan Laboratory, Qingdao, China

as that of the surface current. Besides, Ardhuin et al. (2017) found that mesoscale currents contribute to 75% of the spatial variability in wave height at the scales of 100 km in the Gulf Stream. Similarly, it was found that variability in wave height at scales less than 100 km was well associated with the pattern of current vorticity (Quilfen et al. 2018). As Dysthe (2001) reported, the current vorticity might lead to wave refractions, and accumulation of wave energy resulting from convergence can be an important factor for occurrence of extreme wave height (Quilfen and Chapron 2019). Additionally, ocean currents can affect surface waves indirectly by modifying the effective wind speed at the sea surface (Ardhuin et al. 2012). In the deep ocean, the mesoscale eddy, a common dynamic phenomenon with energetic rotating flows, usually involves in several wave-current processes mentioned above on modulating wave parameters and spectra. With distinct variations in surface waves, sea areas with background mesoscale eddy have been focused on in a number of recent studies (BÜHler and McIntyre 2005; Marechal and de Marez 2021). For example, by investigating a typical eddy in the South China Sea with sensitivity experiments, Wang et al. (2022) reported that mesoscale eddies can alter wave properties (wave height, period and steepness) by 20–30% and wave direction by 30–40°. Another recent study revealed that the shear terms of eddy velocity can modulate wave height and wavelength by 18% and 24%, respectively (Tan et al. 2023).

In open ocean areas, the primary wave influence on ocean currents is the wave-induced current, i.e., Stokes drift (Stokes 1847), attributable to the nonlinearity of waves. As the difference between Lagrangian and Eulerian averages of a flow field, Stokes drift apparently modifies the current field, and by interacting with wind-driven currents, it is considered responsible for the Langmuir circulation in which turbulent motion is transported downward and the water in the upper layers of the ocean is mixed (Craik and Leibovich 1976; McWilliams et al. 1997). Since Stokes drift decays rapidly on the scale of the e-folding depth, its impact is limited to the ocean surface in any case.

Wave-current interactions have been extensively studied through field observations and numerical simulations. Usually, they are more significant by analyzing wave and current data with higher resolutions (Ardhuin et al. 2017; De Carlo et al. 2023; Romero et al. 2020) because more refined wave and current field structures with extreme values are better preserved. However, it does not mean that wave-current interactions should be ignored in large-scale studies. Using global wave simulations, Echevarria et al. (2021) showed marked improvement in modeled wave height by including surface current forcing, even with eddy-permitting configurations. Moreover, Li et al. (2022) also discussed the influence of Stokes drift on maintaining sea surface temperature

stability during Indian Ocean Dipole events. For most of wave-current studies, it can be expected that they usually focused on regions with strong ocean currents, such as the Gulf Stream (Melville et al. 2005; Romero et al. 2017; Wang et al. 1994) and the Agulhas Current, where in situ wave measurements are frequently conducted (Irvine and Tilley 1988; Lavrenov 1998; Quilfen and Chapron 2019). The Kuroshio and its Extension (KE) is another strong western boundary flow system in the Northwest Pacific Ocean with mesoscale eddies on both sides of the flow axis, which should be a typical region for the research on characteristic of wave variations results from background currents. Although the same physical principles can be applied, there are few detailed interpretations of wave-current interactions based on observations conducted in the KE region, except for previous studies that mainly focused on the regulation of wave height by surface currents (Hwang 2005; Hisaki 2023). Hence, more comprehensive analysis based on observational evidence is necessary to enhance our understanding of wave-current interactions and to improve predictions of extreme sea states in the KE region.

In this study, we used data obtained from in situ drifting wave buoys and the China-France Ocean Satellite (CFO-SAT) to quantify the modulating effect of ocean currents on surface waves and the wave-induced Stokes drift in the KE region. The analyses considered various wave parameters and spectra based either on statistics or on selected typical cases. The remainder of this paper is organized as follows. Section 2 introduces the data and methods we used. The bulk wave parameters and the wavenumber spectra influenced by surface currents are described in Sect. 3.1–3.3. The wave-induced Stokes drift is discussed in Sect. 3.4. Finally, the derived conclusions are presented in Sect. 4.

2 Data and methods

Focusing on the KE region (25°–45°N, 130°–180°E), the measurements from both drifting wave buoys and CFO-SAT are extracted to display wave variations and to further interpret the effect of ocean currents. If current velocity and wave direction were not available from field measurements, reanalysis data were adopted instead. Additionally, the drift velocity of wave buoys and Stokes drift determined from reanalysis directional spectrum data were used to evaluate the relative importance of Stokes drift to the surface ocean current.

2.1 Buoy measurements

The buoys used in this study were deployed in the Northwest Pacific Ocean by *R/V Dongfanghong 3* during 2019–2020

Fig. 1 Map of averaged reanalysis current velocity in September 2019 overlaid with trajectories of 10 wave buoys deployed in September 2019 (red lines), November 2019 (magenta lines) and June 2020 (orange lines). Locations of buoy deployment are indicated by black stars

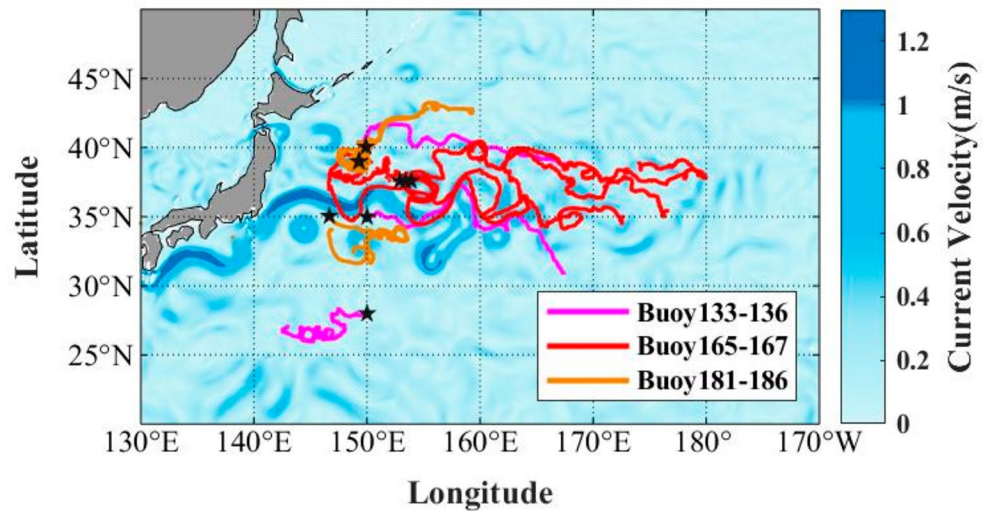


Table 1 Details of the drifting wave buoys deployed

| ID | Date of deployment | Location of deployment | Duration (days) |
|-----|--------------------|------------------------|-----------------|
| 165 | September 8, 2019 | 152.9°E, 37.6°N | 230 |
| 166 | September 8, 2019 | 153.4°E, 37.6°N | 233 |
| 167 | September 8, 2019 | 153.9°E, 37.6°N | 233 |
| 133 | November 10, 2019 | 150.0°E, 35.0°N | 75 |
| 134 | November 8, 2019 | 150.0°E, 40.0°N | 50 |
| 136 | November 13, 2019 | 150.0°E, 28.0°N | 107 |
| 181 | June 17, 2020 | 149.3°E, 39.0°N | 76 |
| 182 | June 17, 2020 | 149.3°E, 39.0°N | 76 |
| 183 | June 21, 2020 | 146.7°E, 35.0°N | 72 |
| 186 | June 21, 2020 | 146.7°E, 35.0°N | 72 |

as a part of a KE observational campaign. Each buoy comprised a nine-component acceleration sensor with 0.4-m diameter and total weight of 11 kg for easy deployment and rapid in situ observations. The performance of this type of wave buoy was verified against that of a Waverider buoy (Cheng et al. 2022). The Significant wave height (SWH) with 1-h sampling resolution was obtained from 10 drifting wave buoys. The SWH adopts the average of the first third of wave heights, which is almost the same as that calculated by $4.005\sqrt{m_0}$ within the observed wave frequency range (0.0078–0.5 Hz), where m_0 represents the zero moment of wave spectrum. The tracks of the undrogued buoys are shown in Fig. 1 and the details of deployments are listed in Table 1.

2.2 Along-track altimeter data

The CFOSAT launched on 29 October 2018 carries a wind scatterometer and a SWIM wave spectrometer with swath width of approximately 1000 and 180 km, respectively. It provides simultaneous and collocated observations of sea surface wind and wave fields with spatial resolution of 12.5×12.5 and 70×90 km, respectively. On the basis of the

two-dimensional directional wave spectrum calculated from the “wave box” on both sides of the CFOSAT track, ground data processing centers use special algorithms to extract bulk wave parameters, including SWH, dominant wavelength and wave direction either from the entire combined spectrum or from the partitioned wave spectrum (Hauser et al. 2021; Xu et al. 2019). The SWIM data we used is version 5.1.2. Since the polar-symmetric configuration renders the wave spectrum incapable of discerning whether the wave is propagating toward or away from a particular direction, it includes a 180° ambiguity (Hauser et al. 2017). Thus, we corrected the dominant wave direction using the reanalysis data described in Sect. 2.3, i.e., it is corrected by adding or subtracting 180° if it is not in the same quadrant of the reanalysis wave direction. Nadir observations of SWH from altimeter and wind speed from scatterometer with higher spatial resolution of about 8 km and 1.5 km are also used for analysis. Comparison of the nadir SWH from September–December 2019 with the reanalysis data (Sect. 2.3) revealed a mean relative deviation of 6.6%, thereby confirming the reliability of the two types of data.

2.3 Reanalysis data

Since the observed velocity of surface current is not available for such a large area, the 3-hourly reanalyzed ocean surface currents are used if necessary. The current data were derived from the GLORYS12V1 product based on ERA5 reanalysis in combination with altimeter measurements before June 2020, and then updated by the GLO12v3 product, both of which are provided by the Copernicus Marine Service (CMEMS) with $1/12^\circ$ resolution. Notably, the current can be regarded as at least the combination of wind, geostrophic, and inertial currents; therefore, it is expected to be close to the real background current.

Similarly, the wave parameters, i.e., SWH, peak wave period, mean wave direction, peak wave direction and Stokes drift data, covering the KE were obtained from the global surface $1/5^\circ$ product with a 3-hour interval based on the Météo-France wave model (MFWAM) provided by the CMEMS. To investigate the wind effects in typical cases, we also used the WIND_GLO_PHY_L4_NRT_012_004 hourly sea surface wind speed product with $1/8^\circ$ resolution provided by the CMEMS.

The daily gridded level-4 sea level anomaly (SLA) with $1/4^\circ$ resolution, obtained from the Data Unification and Altimeter Combination System product provided by the CMEMS, was used to detect mesoscale eddies. In this product, the SLA is estimated using optimal interpolation of merged L3 along-track measurements from different altimeter missions.

3 Results and discussions

3.1 Variation in wave height with currents

To display the variations in surface waves with background ocean currents in the KE, several correlations between quantities related to wave height and current velocity are investigated. Firstly, focusing on flow axis regions with relatively stable and strong currents, two typical cases on 27 November 2019 and 1 December 2019 are shown in Fig. 2a and c, respectively. In each case, the altimeter crossed the flow axis with one buoy located nearby. By collecting the SWHs and surface current vectors at the buoy location and along the altimeter track on the day, the joint distributions of SWH and the angle between the propagation directions of waves and currents (hereafter, A , range: 0° – 180°) are shown in Fig. 2b and d. According to the reanalyzed wind product, the wind speed vectors for these two cases changes small indicating relatively steady wind fields. Thus, the impact of the

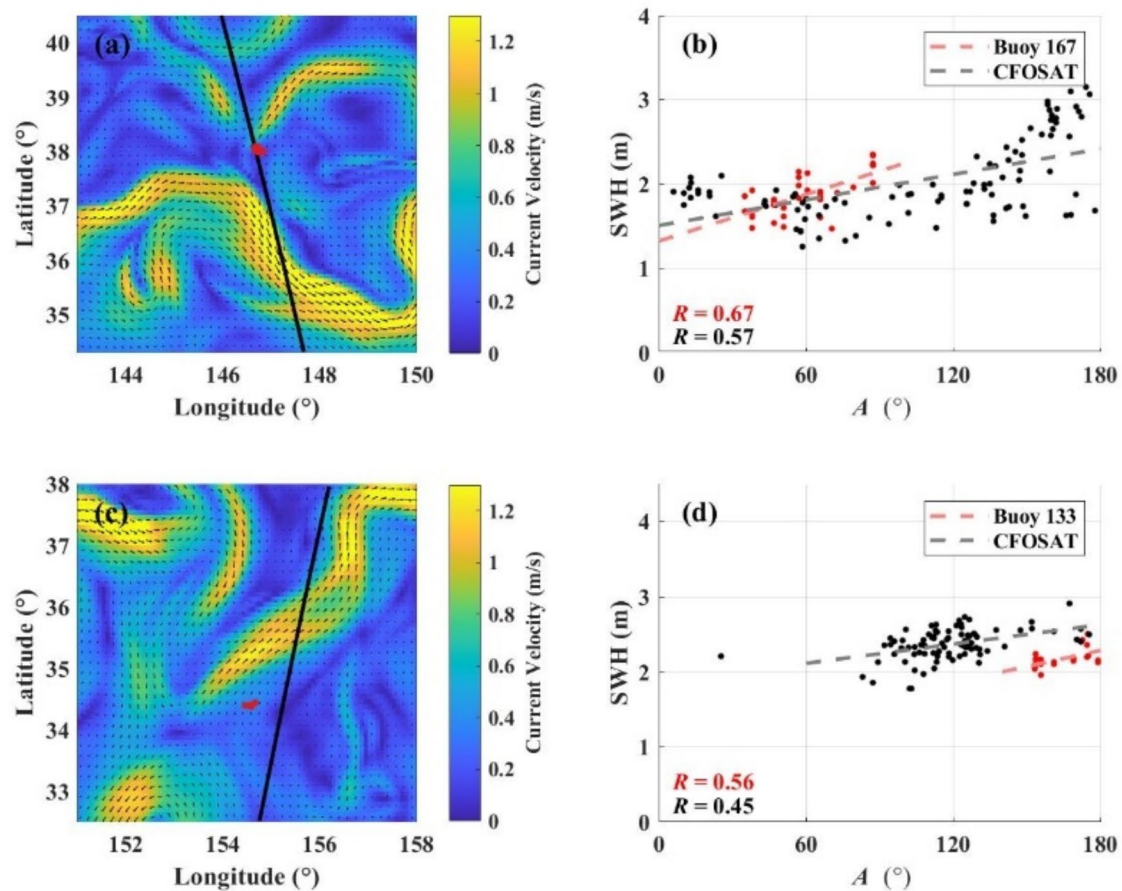


Fig. 2 CFOSAT trajectory (black lines) and buoy locations (red dots) with background current on (a) 27 November 2019 and (c) 1 December 2019, respectively. (b) and (d) are the corresponding SWH as a function of A with the R in the left bottom

ocean currents on the surface waves was less contaminated by the sea surface wind. Furthermore, no accidental extreme wave height was found in the reanalysis SWH field.

For the cases selected, it is evident that the SWH increases with increasing A for both the altimeter and the buoy measurements. And the latter shows larger correlation coefficients R reached 0.67 for the case on 27 November 2019. If a linear least square fitting is performed to roughly describe the relationship, the slope of the fitting line is greater for the buoy data at a smaller scale with a higher spatial resolution. Generally, the relation between SWH and A is consistent with that reported in previous studies (Hwang 2005; Romero et al. 2017; Wang et al. 2020), and the variation in SWH from CFOSAT shown in Fig. 2b is comparable to that observed by Romero et al. (2017) in the Gulf of Mexico, i.e., 0.30 m with a 180° change in A .

Of note, it is hard to capture a perfect regular wave propagating across the KE and any other sea areas in the field as well. Although the effects of wind are artificially minimized by selecting cases with stable sea surface winds, the presented SWH with variation in A remains affected by the inhomogeneity of the ocean waves, e.g., the variance induced by wave groups (De Carlo et al. 2023). From another perspective, analyzing wave and current field data at different scales might lead to different results quantitatively, which is confirmed by the differences in the rate of SWH change with A between the buoy and the altimeter measurements, but the positive relation remains consistent qualitatively. Except for two specific cases discussed above, we further statistically investigate the changes in SWH and perform spatial spectral analysis of the SWH to show the general features of wave heights regulated by currents in the KE region.

Based on statistical analysis, random influences on the variation in SWH can be well excluded. Hence, all measured SWHs of buoys 165, 166, and 167 with relatively long drifting distances and time series are compared with the reanalyzed SWH to verify whether the effect of A on SWH is still significant in the KE region. Though the reanalysis wave data based on the MFWAM are assimilated using field observations, which implies that the current effects on waves are contained within the data to some extent. It is believed that those effects are not fully represented because they are not considered in the simulation with the MFWAM itself (Hisaki 2023). Therefore, it is expected that the variation in SWH resulted from currents can be reflected by the difference between buoy-measured and reanalyzed SWH. To do so, the average bias B was first calculated as follows:

$$B = \frac{1}{n} \sum_{i=1}^n (H_{ri} - H_{oi}) \tag{1}$$

where H_{ri} and H_{oi} are the reanalysis and observed SWH at buoy locations, respectively, subscript i denotes each observing point, and n is the total number of observations. Next, to examine the effect of ocean currents on wave height, two types of difference, D (excluding the effect of the mean deviation) and P (relative to the observation), are defined as follows:

$$D_i = H_{ri} - H_{oi} - B \tag{2}$$

$$P_i = \frac{D_i}{H_{oi}} \times 100\% \tag{3}$$

The calculated D and P versus A are shown in Fig. 3. Generally, the reanalysis SWHs are higher (lower) than the observations when the waves and currents are in the same (opposite) directions. The linear fits of averaged values of both D and P for each bin of A with a 15° interval are characterized by negative slopes, depicting the statistical relationship of wave height deviations and the angle between waves and currents. Specifically, when A is 0° , i.e., the directions of waves and currents are the same, the reanalysis SWH is 0.10 m (approximately 3%) higher on average than that observed. When waves and currents are in opposite directions, i.e., $A = 180^\circ$, the reanalysis SWH is 0.11 m (approximately 4%) lower than that observed. As expected, the variation in SWH with change in A is lower than the value of 5–7% reported by Cheng et al. (2022) who adopted unassimilated model data. However, it confirms that even reanalysis wave data with assimilation cannot fully represent the current effects on waves in the KE region. For example, variations in SWH, resulting from the relative directions between surface waves and currents, are accounted for by both the direct influence of the Doppler shift through maintaining wave action conservation and the indirect influence of regulating relative wind.

Besides displaying the relationship between SWH and A at selected buoy locations, we further investigate the spatial wavenumber spectra of SWH and surface current velocity along the satellite trajectory using Fourier transforms. To do so, we analyzed a series of cases from 1 September to 31 December 2019. In each case, we selected a 6-latitudes part of altimeter tracks crossing the current axis where current effects on waves are expected to be notable, and the distance to adjacent observing points was approximately 8 km. Then the resolvable wavenumbers were for $k = 0.003\text{--}0.063$ cycles/km (scales of 16–375 km). The current velocity is interpolated from reanalysis data to the altimeter tracks. For the cases investigated, the behaviors of wave and current spectra are not always similar though the background current keeps stable and strong. It implies that sometimes the wind-wave generation dominate the regional

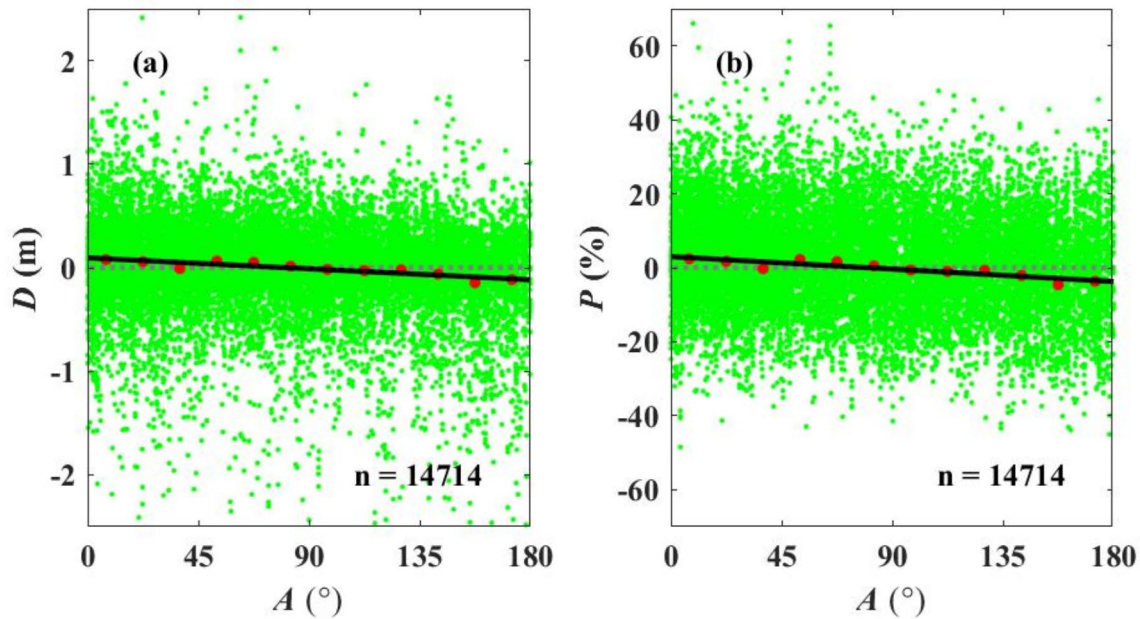


Fig. 3 (a) D and (b) P as a function of A . Red dots denote averaged values for each 15° bin, and the solid line is their linear fit which has passed the significance test with a confidence level of 95%

distribution of SWH to a great degree. To verify it, the wave age β defined as: $\beta = \frac{C_p}{U_{10}}$ is applied to judge the dominance of wind-wave or swell, where U_{10} is the 10-m wind speed and $C_p = \frac{gT_p}{2\pi}$ is the phase velocity of the dominant wave component with the peak wave period T_p . Generally, cases with bad correlations between the SWH and current velocity spectrum are wind-wave dominated, i.e., $\beta < 1.2$ (Komen et al. 1994). For example, on 12 September 2019, the SWH spectrum is highly related to the wind speed spectrum at almost all the scales distinguished, while it is not to the current velocity spectrum as Fig. 4c and d shows. On the contrary, when swell is dominant, e.g., the case shown in Fig. 4a, the two spectra of SWH and current velocity display a considerable similarity. As the shaded section shows in Fig. 4b, there is a clear correspondence between the SWH and current velocity spectrum at scales of 18–191 km. Compared with wind-wave cases, it is more likely to extract the current-induced modulation on spatial distribution of SWH from swell-dominated cases in the KE region as the wind-induced variation in SWH is less significant.

For the scale of mesoscale currents, the strong correlation between SWH and current speed shown here has also been confirmed in numerical studies of the Gulf Stream. The power law slopes of the two spectra in Fig. 4b are approximately -2 to -3 , which is same as that reported by Arduin et al. (2017), implying the spatial variabilities of waves and currents in the KE region are comparable to those in the Gulf Stream. Notably, as the wavenumber increases to larger

values (at scales < 20 km), the behaviors of the two spectra no longer exhibit strong correlation. On the one hand, the spatial variation in SWH is closely associated with-wave groups at scales smaller than 20 km (De Carlo et al. 2023). On the other hand, the accuracy of the spectra is reduced because the wavenumber is close to the Nyquist wavenumber. Hence, we remain caution to interpret the current effects on waves with the presented data at scales less than 20 km. Similarly, the accuracies of the spectra at very small wavenumbers are also limited by the length of the selected track.

Apart from the angle between wave and current directions (A) and the current velocity, wave height variability is also believed to be well associated with the vorticity of the background current field (Quilfen et al. 2018; Romero et al. 2020). From a statistical perspective based on numerical simulation data, Villas Bôas et al. (2020) proposed a positive relationship between the spatial gradients of SWH and the vertical vorticity of surface current for narrow-banded swell that can be expressed as follows:

$$C_g \frac{|\nabla H_s|_{RMS}}{\langle H_s \rangle} \propto \mathcal{S} \zeta_{RMS} \quad (4)$$

where C_g is the group velocity of waves determined by $C_g = \frac{gT_p}{4\pi}$, $\langle \nabla H_s \rangle_{RMS}$ is the root mean square (RMS) SWH gradient, $\langle H_s \rangle$ is the mean SWH, \mathcal{S} is the spectral slope of the currents and ζ_{RMS} is the RMS vertical vorticity of the current. These parameters can be calculated based on altimeter-derived SWH and reanalysis current velocity

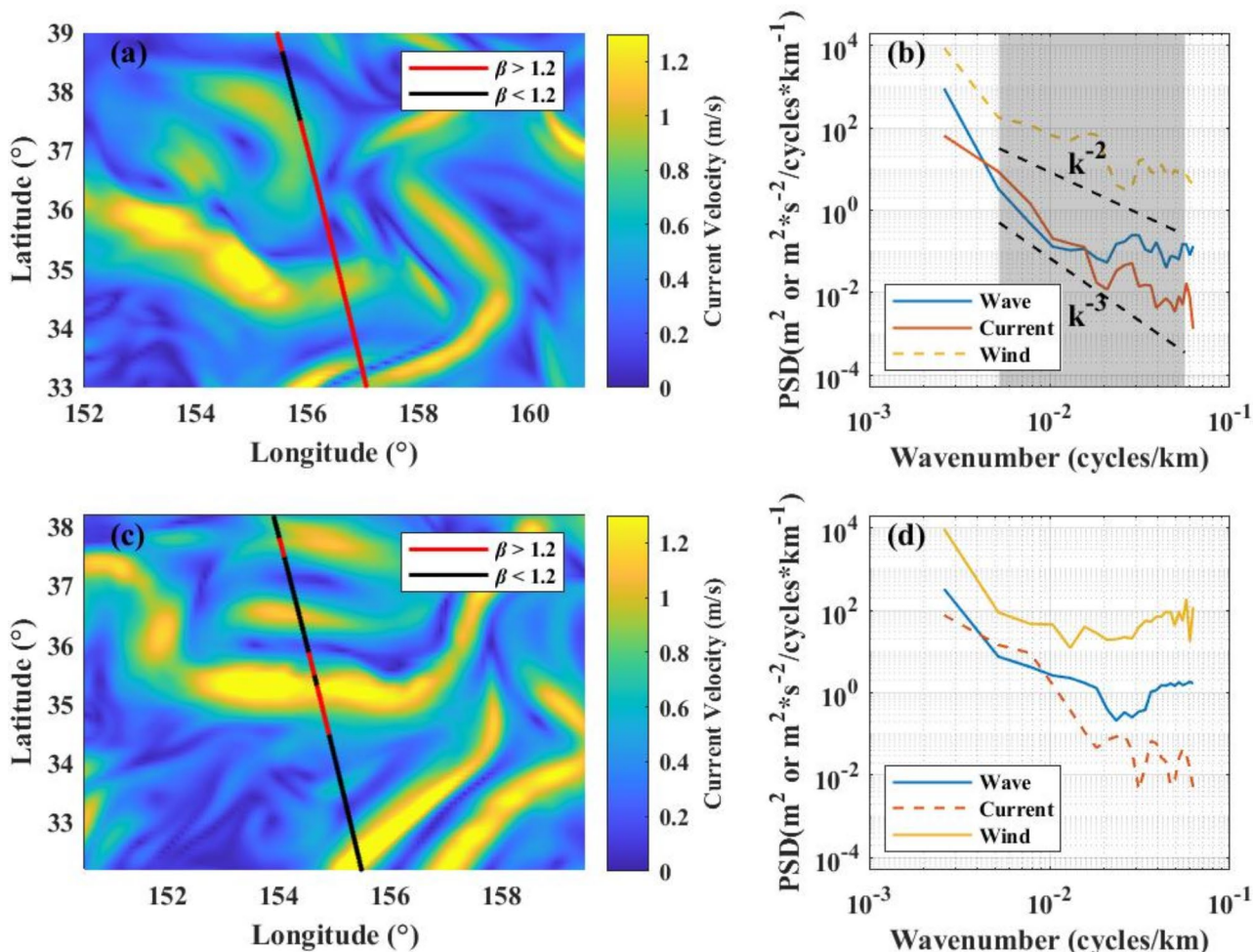


Fig. 4 (a) Current velocity with CFOSAT trajectory. Black and red lines represent wind-wave and swell dominance, respectively. (b) Wavenumber spectra of SWH, current velocity and wind speed with

and peak wave period T_p . Here, data along CFOSAT tracks on each day from July to December 2019 are considered to check the applicability of Eq. (4) in the KE region (30°–40°N, 140°–160°E). On each day, C_g is the averaged group velocity along each track, and S is the approximate power law slope of the current spectrum, with approximately 85% of its values ranging from -3 to -2 as shown in Fig. 4b and d. As shown in Fig. 5, the boxplot of the relation between $C_g \frac{|\nabla H_s|_{RMS}}{H_s}$ and $S\zeta_{RMS}$ partially confirms the regulation of the wave height gradient attributable to current vorticity. In fact, the linear relationship between these two terms for each case is not as robust as that found by Villas Bôas et al. (2020). On one hand, methods of approximation adopted to determine C_g and S will introduce uncertainties. On the other hand, Eq. (4) is designed for narrow-banded swell which ignores wind forcing, it might not be fully applicable to wind-driven waves in the KE region. If only the swell-dominated cases ($\beta > 1.2$) are focused, the

approximate power laws on 19 September 2019. (c) and (d) are same as (a) and (b), respectively, but for 12 September 2019

linear relationship will be more robust with smaller standard deviation for each bin of $S\zeta_{RMS}$. In general, the fit of medians shows a clear positive linear relationship which indicates the nonnegligible influence of current vorticity on the spatial gradients of SWH.

3.2 Variations in wave parameters across eddies

Mesoscale eddies in the global ocean can substantially modulate the features of ocean waves (Marechal and de Marez 2021; Wang et al. 2022), and the KE region is an area rich in vortex systems. To quantify the influence of eddies on ocean waves, we identified 45 tracks in a 6-month period (September 2019 to February 2020) of SWIM data that passed over mesoscale eddies in the KE region; 25 (20) tracks passed over cold (warm) eddies. Here, we ignored cases of eddies affected by local strong wind systems, e.g., typhoons. The “wave box” grids along the track were classified into two

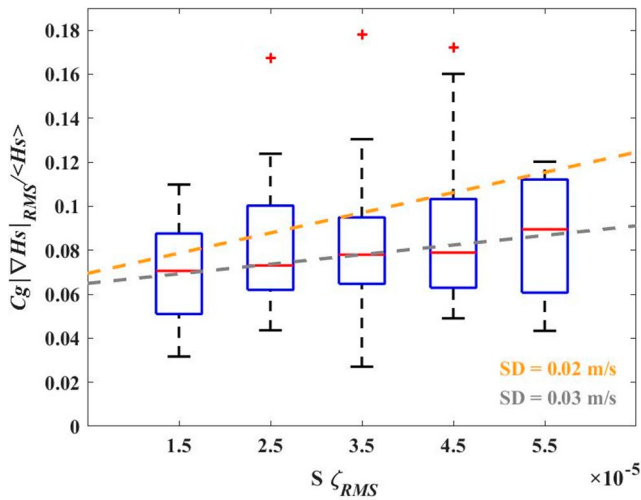


Fig. 5 Boxplot of $C_g \frac{|\nabla H_s|_{RMS}}{\langle H_s \rangle}$ as a function of $S \zeta_{RMS}$. Grey and orange dashed lines represent the linear fitting lines of medians for all cases and swell-dominated cases, respectively, with corresponding mean standard deviation (SD) values for each bin of $S \zeta_{RMS}$. The two fitting lines have both passed the significant test with a 95% confidence

types according to their location: outside or inside the eddy. As shown in Fig. 6, the outermost closed SLA contour was taken as the eddy boundary, the area with homogeneous vorticity was defined as the inside of the eddy, and the outside of the eddy was considered the area with changing vorticity but not in another eddy.

As reported in previous studies, surface waves might behave differently when propagating through cold and warm eddies owing to the different thermal and dynamic structures at the air–sea interface (Chelton and Xie 2010). Hence, we analyze the variations in wave parameters across cold and

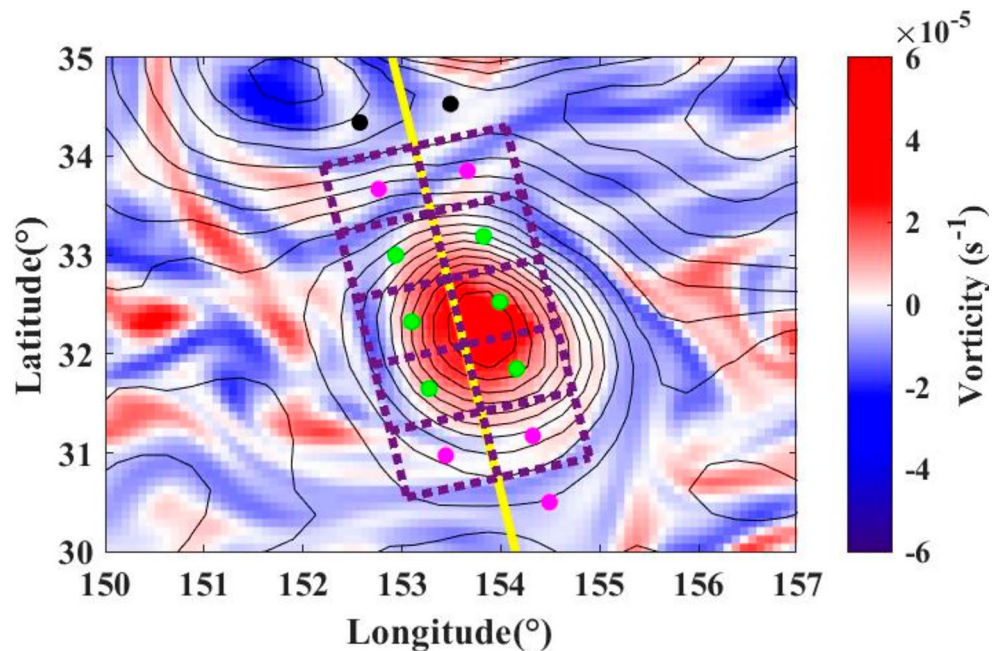
Table 2 Mean variations in wave parameters and wind speed at different eddy locations

| Parameters | Eddy locations | Warm eddies | Cold eddies |
|------------------|------------------|-------------|----------------|
| SWH (m) | Inside | 2.94 | 2.87 |
| | Outside | 2.80 | 2.99 |
| | Inside – Outside | 0.14 (5%) | -0.12 (-4%) |
| Wavelength (m) | Inside | 184 | 195 |
| | Outside | 169 | 203 |
| | Inside – Outside | 15 (8%) | -8 (-4%) |
| Wind speed (m/s) | Inside | 11.55 | 9.91 |
| | Outside | 10.88 | 10.17 |
| | Inside – Outside | 0.67 (6%) | -0.25 (-3%) |
| Deflection (°) | \ | -11 | 11 (clockwise) |

warm eddies separately. We collected the SWH, dominant wavelength, wave direction (increasing clockwise from geographic north) and wind speed both inside and outside each eddy and investigated their variations. All of the wave data were determined from the entire combined spectrum from the SWIM. Among them, variations in wave direction were determined as the difference between the direction of wave groups entering an eddy and that of wave groups leaving an eddy. And the average statistics are shown in Table 2.

The results indicated that the mean SWH of warm eddies is higher inside the eddy on average, whereas the converse is true for cold eddies. The absolute values of the relative deviation between the inside and the outside of warm and cold eddies show no big difference (around 5%). Correspondingly, the mean dominant wavelength is higher (lower) inside warm (cold) eddies, and the absolute difference between the inside and the outside of warm (cold) eddies are approximately 8% (4%). For the wave direction, generally, it exhibits a tendency to increase clockwise when

Fig. 6 Illustration of the definition of different eddy locations. Yellow line represents the CFO-SAT trajectory on 30 September 2019 with the “wave boxes” observed by the SWIM shown in purple. Green and magenta dots identify boxes that are inside and outside the eddy, respectively. Background colors represent surface current vorticity with contours of the SLA



waves are propagating through a cold eddy, whereas the deflection is in the opposite sense for a warm eddy. Such curvature can be explained by the wave refraction induced by local vorticity (Dysthe 2001), i.e., the wave direction will be deflected clockwise (anticlockwise) by traveling through a region with positive (negative) vorticity. On average, the deflection is approximately 11° which is comparable to the values found in the South China Sea, however, the relative variation in SWH found in this study is approximately one-third as a percentage compared to that reported in Tan et al. (2023). The relatively small variation in SWH in the KE region is probably attributable to stronger waves (three times larger in terms of SWH) with higher wind-wave fractions and stronger wave breaking implying a more complex situation involving multiple mechanisms.

From another point of view, this result shows the waves in warm eddies are generally stronger than those in cold eddies, which can be well explained by the stronger winds in warm eddies as shown in Table 2, i.e., the cyclonic eddies will slacken near-surface winds (Frenger et al. 2013). However, it should be noted that it is a statistical result for 45 cases in the KE region. In a specific case, waves may not follow the general behavior propagating through an eddy. For clarification, a case on 8 October 2019 with westward waves travelling through a cold eddy located at $154^\circ\text{--}156^\circ\text{E}$, $31^\circ\text{--}33^\circ\text{N}$ is selected to display the difference of SWH between the inside and outside of the eddy, which is shown in Fig. 7. According to the results shown in Fig. 7b and c, it is found that the average SWH inside the eddy (2.0 m) is larger than that outside the eddy (1.9 m) though the average wind speed is smaller (3.7 m/s) inside than the

outside (4.5 m/s). Moreover, the general trend of variation in SWH is opposite to that in wind speed along the track. For example, at the north edge of the eddy, weaker waves are corresponding to stronger winds compared to those at the south edge of the eddy. So, apparently, it is a typical situation discussed in Sect. 3.1, i.e., the variation in A tends to become the primary factor leading to wave variability.

In the KE region, different from an ideal experiment, the observed waves usually experience multiple effects related to mesoscale eddies. The existence of these physical processes, at least the eddy-induced modulation of the surface wind, variation in A , and refraction mentioned subsequently, ultimately determines the complexity of wave variability. Under different situations or with different methods of data analysis, many of these mechanisms could become important. However, the statistical average corresponds to the wind strength regulated by the polarity of eddies because a variety of influencing factors can be regarded as random processes which are equivalent for the two types of eddies.

3.3 Wave refraction by currents

Wave refraction, which is a typical phenomenon that occurs when surface waves propagate through a field with background currents in the ocean, has been both observed and modeled in previous studies (Kenyon 1971; Peregrine 1976; Quilfen and Chapron 2019). The detailed theory of refraction can be found in Dysthe (2001). The main two assumptions are as follows: (1) the current field is considered time-independent during swell propagation, and (2) the swell does not dissipate when it travels through the current

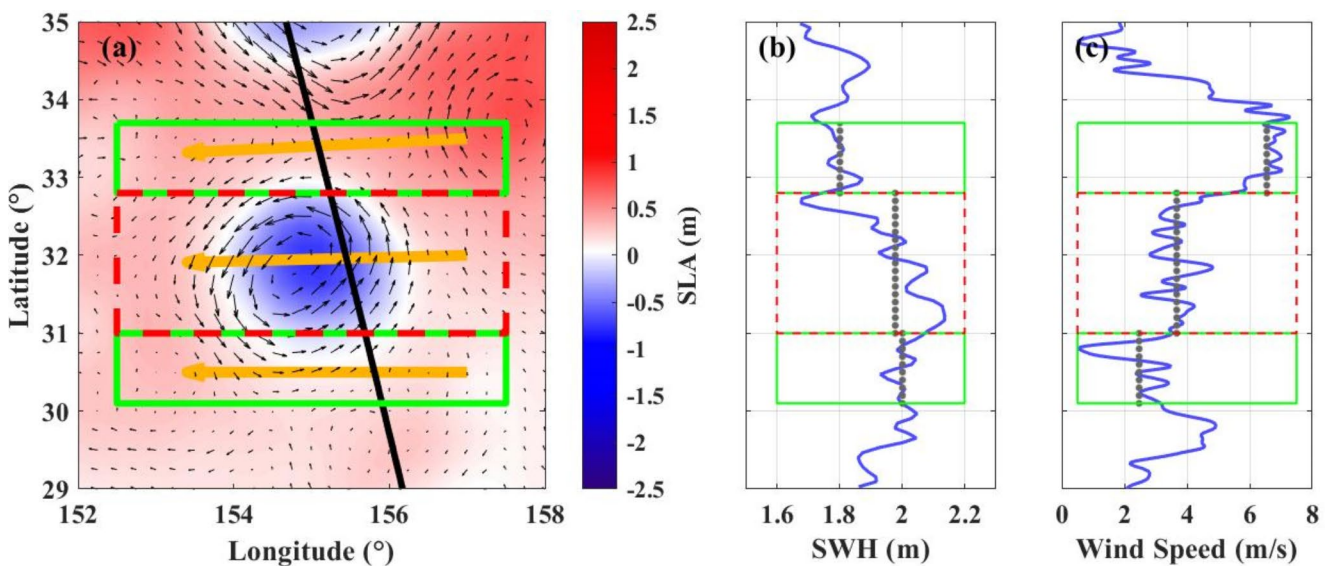


Fig. 7 (a) A cold eddy in the KE region with the SWIM track (black line). Colored shading, black and orange arrows represent the SLA, current and wave forward directions, respectively. The green and red boxes represent outside and inside regions of the eddy, respectively.

(b) Smoothed SWH and (c) wind speed along the SWIM track on 8 October 2019 with grey dashed lines representing the mean values within boxes

system. The governing equation of wave trains can be expressed as follows:

$$\frac{dx}{dt} = \frac{\partial \Omega}{\partial k}, \quad \frac{dk}{dt} = -\frac{\partial \Omega}{\partial x} \tag{5}$$

where $\Omega(k, x) = \sqrt{gk} + k \bullet U$ is the dispersion relation for gravity waves in deep water, and k and U are the surface wave and current vector, respectively. The angle of ray curvature ϕ is given by the following (Quilfen and Chapron 2019):

$$\phi = \frac{\zeta l}{C_g} \tag{6}$$

where ζ is the vertical vorticity of the surface current, and l is the distance traveled by the swell trains with the wave group velocity C_g .

Owing to notable ray deflection, localized sea state gradients can be anticipated and well traced in altimeter signals (Quilfen et al. 2018). To display wave refraction in the KE region, two cases with relative steady wave fields and one altimeter trajectory were selected as examples to predict the wave refraction. One case shown in Fig. 8a–c is at 12:00 UTC on 7 September 2019. The swell came from the southeastern area outside the region and traveled for 2 days with a forward angle of 310° relative to north and peak wavelength of 90 m. The waves traveled through the KE region with a group velocity of 6.0 m/s, and the maximum surface current velocity met along the flow axis was approximately 2.0 m/s. On the basis of Eq. (6), the predicted rays are shown in Fig. 8c with the accumulated angle of wave deflection reaching 40° while propagating approximately 200 km. Similar to Quilfen et al. (2018), we selected data from the altimeter track across the same region during period of travel of the swell train to extract evidence of

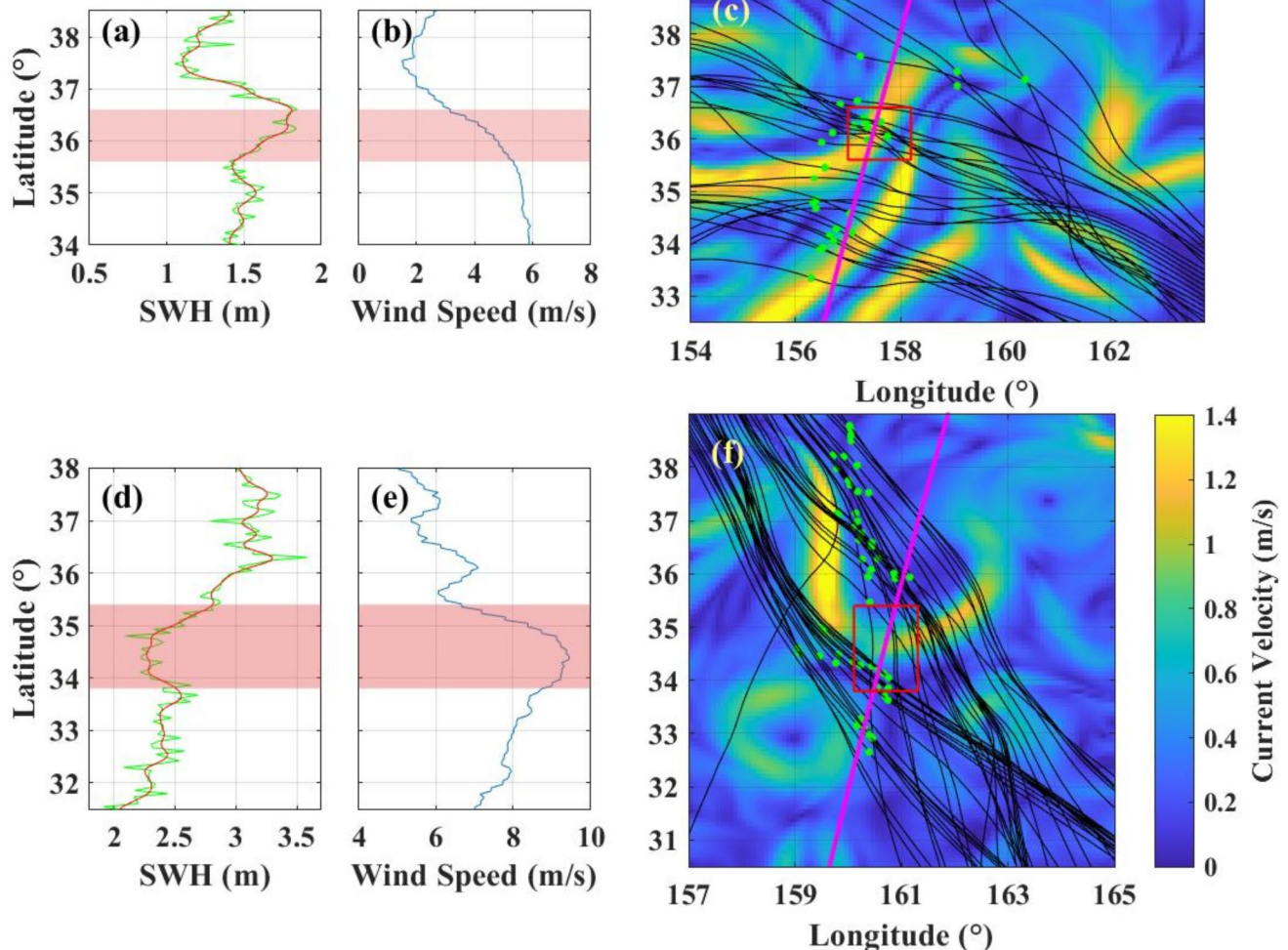


Fig. 8 (a) SWH (smoothed in red line) and (b) wind speed as a function of latitude. (c) Predicted rays overlaid on current velocity on 8 September 2019. Magenta line represents the altimeter trajectory and

green dots represent the predicted locations of the swell when the altimeter passed over the region. (d)–(f) Same as (a)–(c), but on 22 December 2019

swell convergence and divergence. On 8 September 2019, the waves propagated to a region (green dots) near the trajectory of the CFOSAT track. By collecting observed SWH and wind speed data along the track, which are shown in Fig. 8a and b as a function of latitude, it can be found that the SWH near 36.5°N is approximately 0.3 m larger than that both at around one latitude north or south even the sea surface wind is higher at south. However, according to the predicted wave rays, convergence occurred from 35.6°N to 36.6°N (red shadows in Fig. 8a–b), which could explain the observed local high SWH.

Another case of swell coming from the northwest of the KE region is shown in Fig. 8d–f. As the swell propagated from the northwest toward the southeast with a group velocity of 8.2 m/s, it probably reached the location of the altimeter track on 22 December 2019. Along the track, the variation in observed SWH generally follows that of wind speed, except for the section from 33.8°N to 35.4°N (red shadows in Fig. 8d–e), where a local minimum in SWH, approximately 0.4 m smaller than the north and south sides of the area, corresponds to a local maximum in wind speed. Analogous to the previous example, divergence occurred in the middle of the region according to the predicted wave rays. Thus, it makes sense that the wave energy is locally lower with stronger surface winds.

Since SWH in the open ocean is undoubtedly influenced by local winds, the convergence and divergence of wave rays that we predicted cannot always fit the variability in SWH exactly; however, it still provides a method to help us detect possible wave anomalies. The above-observed evidence shows that swell can undergo marked refraction in the KE region where the background currents are strong and complex. The bending of wave rays will result in convergence and divergence of wave energy introducing greater variability in the wave fields, which could be more than 0.4 m as the above case shows. Such magnitude of wave refractions has also been verified in simulations and observations in other regions with energetic mesoscale variability, e.g., the Agulhas Current (Kudryavtsev et al. 2017; Quilfen et al. 2018). In other words, it would cause greater uncertainty in wave forecasts based solely on sea surface winds.

3.4 Wave-induced Stokes drift

Surface waves can affect currents in several ways and even some of them are indirect. In this part, we focus on the most direct influence that waves have on surface currents, i.e., Stokes drift. Stokes drift, which decays rapidly on the scale of the e-folding depth, is regarded as the difference between the Lagrangian and Eulerian averages of a flow field (van den Bremer & Breivik, 2018). With respect to the KE region, Stokes drift has rarely been discussed, especially in

relation to in situ measurements. Therefore, for the purpose of displaying more information with the available data, we combined drifting buoy data and reanalysis data to quantify the relative importance of surface Stokes drift to ocean currents, and to verify whether surface currents are better estimated when considering the surface Stokes drift.

For deep water, Stokes drift can be calculated using bulk wave parameters, which can be defined as follows (Tamura et al. 2012):

$$U_b = g^{-1} \pi^3 H_s^2 T_p^{-3} \tag{7}$$

where g is gravitational acceleration, H_s is SWH, and T_p is the peak wave period. Stokes drift can also be estimated using a wave spectrum, which is widely believed to have higher accuracy (Webb and Fox-Kemper 2015) and can be defined as follows (Breivik et al. 2014):

$$U_s = \frac{16\pi^3}{g} \int_0^{2\pi} \int_0^\infty f^3 \mathbf{k} F(f, \theta) df d\theta \tag{8}$$

where \mathbf{k} is the unit vector in the direction of the wave component wavenumber, and $F(f, \theta)$ is the frequency directional spectrum with an f^{-5} spectral tail.

Both methods were used to calculate Stokes drift values at the buoy locations, which were then compared to the reanalysis surface currents. Because the buoy was designed to reduce the leeway speed which should be less than 1% of the wind speed according to the estimation in Poulain et al. (2009), it is a good indicator of the actual surface current, the time and location information recorded by the buoys can be used to directly estimate the surface velocity in the field. As examples, four kinds of surface velocity at locations of buoy 134, 165, and 181 are shown in Fig. 9. For clearer expression, C_r and C_b are defined as the sea surface current velocity from the reanalysis data and estimated from the buoy tracks, respectively. The latter is also regarded as the real current velocity at the sea surface. It is evident that the reanalysis current velocity C_r vectorially together with the Stokes drift estimated by the wave spectrum U_s , which is usually larger than that estimated by bulk wave parameters U_b , is the closest to the actual sea surface current C_b most of the time (i.e., 59%, 63%, and 52% of the time for buoy 134, 165, and 181, respectively). Besides, the averaged ratio of U_s to C_r is 49%, 59%, and 25% for buoy 134, 165, and 181, respectively, and 54% for the total average, thereby indicating the considerable importance of U_s for evaluating the surface current in the KE region. By the way, because the temporal resolution of the buoy location data is higher than that of the reanalysis data, the fluctuations in the time series of C_b are more notable than those in the other three series.

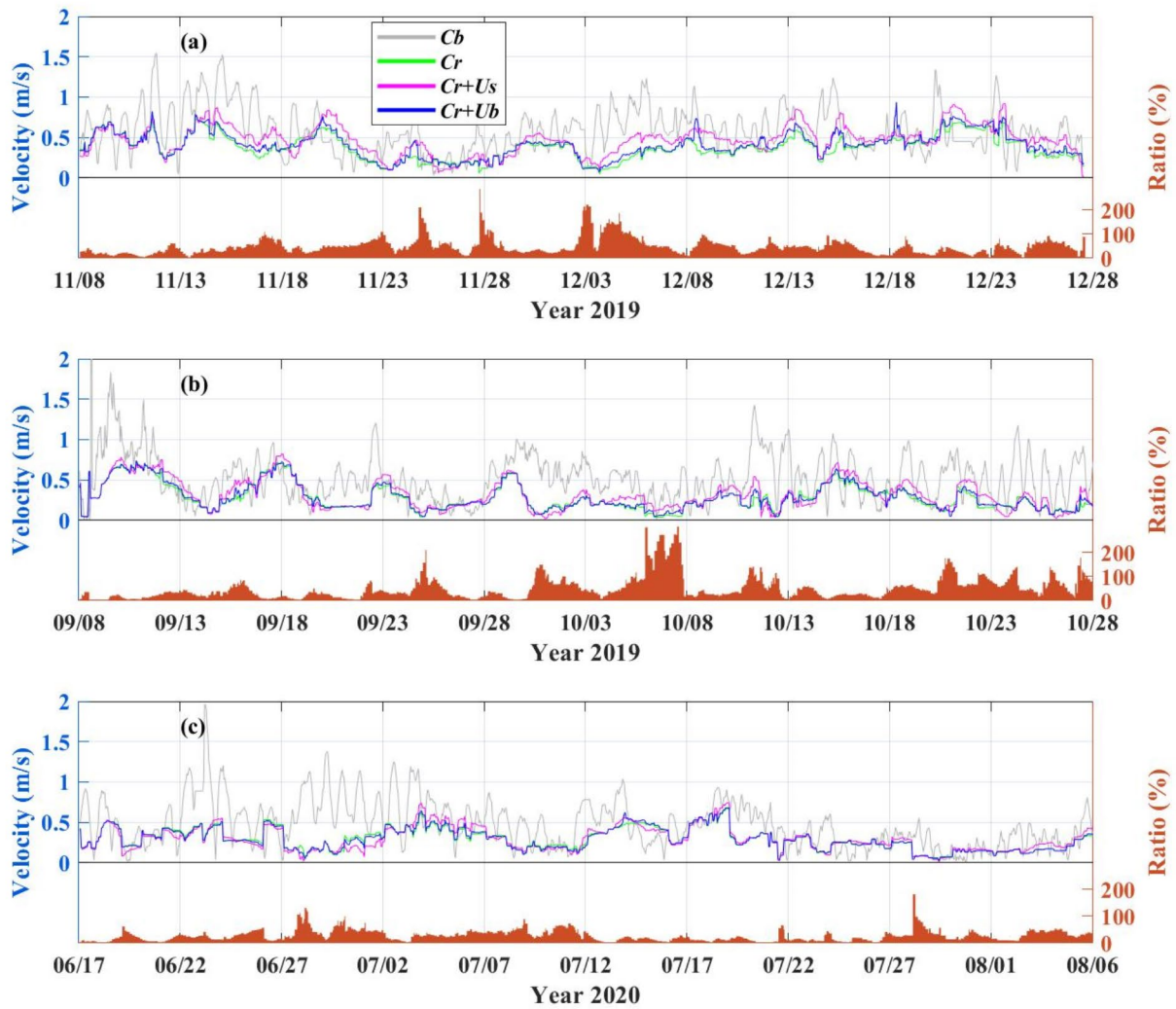


Fig. 9 Comparisons of C_b (gray), C_r (green), $C_r + U_s$ (magenta), and $C_r + U_b$ (blue) for buoy (a) 134, (b) 165, and (c) 181. Orange bars in the bottom represent the ratio of U_s to C_r

To evaluate the importance of Stokes drift to the surface current in the KE region in details, we define D_r as the relative error between C_r and C_b , and D_s as the relative error between $C_r + U_s$ and C_b .

$$D_r = \frac{|C_b - C_r|}{C_b} \times 100\% \tag{9}$$

$$D_s = \frac{|C_b - (C_r \mp U_s)|}{C_b} \times 100\% \tag{10}$$

The statistical results for all selected buoys are presented in Table 3. By vectorially combining C_r and U_s , the accuracy of the surface current estimation is improved on average.

The mean percentage of cases with $D_s < D_r$ is 55% of the total and up to 62% for buoy 134. For all cases, the improvement in accuracy of the surface currents estimation $D_r - D_s$ is approximately 4% and up to 14% if we focus only on cases with $D_s < D_r$ cases. Besides the magnitude of velocity, the change of surface current direction is also evaluated. As shown in Table 3, if C_r is with U_s , the current direction is improved for 56% of the total cases. And it is up to 64% for buoy 136. These results mean that the estimation of surface currents will be improved by further considering the Stokes drift derived from wave spectra. Furthermore, if the results are categorized into different regions, it is evident that the improvement is greater in sea areas without a flow axis and eddies, i.e., smaller background currents. And by

Table 3 Contribution of Stokes drift to the surface currents for each buoy

| Buoy ID | 133 | 134 | 136 | 165 | 166 | 167 | 181 | 182 | 183 | 186 | Weighted average |
|---|-----|-----|-----|-----|-----|-----|-----|-----|-----|-----|------------------|
| Ratio of U_s to C_r | 74% | 49% | 95% | 59% | 48% | 54% | 25% | 34% | 53% | 36% | 54% |
| Percentage of $D_s < D_r$ cases | 56% | 62% | 61% | 57% | 52% | 56% | 44% | 51% | 53% | 57% | 55% |
| Percentage of Mean $D_r - D_s$ | 7% | 5% | 7% | 5% | 3% | 3% | 0% | 1% | 3% | 3% | 4% |
| all cases | 20% | 17% | 18% | 16% | 15% | 14% | 9% | 10% | 9% | 10% | 14% |
| $D_s < D_r$ cases | 62% | 53% | 64% | 50% | 48% | 60% | 47% | 53% | 60% | 62% | 56% |
| Percentage of cases with improved current direction | | | | | | | | | | | |

comparison, the Stokes drift in the eastern KE region contributes more to the surface current than that in the west, mainly because of stronger waves associated with the longer fetch of the westerlies.

4 Conclusions

Wave-current interactions have long been a popular research topic. A number of theories, which is usually considered universal, have been proposed to interpret the observed wave variations attributable to their interactions, and to quantify the wave-current coupling effects in numerical models. In the real ocean, the behaviors of surface waves influenced by currents manifest differently in different areas and on different spatiotemporal scales. In this study, focusing on the KE region, we quantified the surface wave variations relating to ocean currents based on drifting buoy data and CFOSAT observations acquired during 2019–2020. The main findings are summarized below.

1. Under relatively stable wind conditions, the buoy-measured and altimeter-derived SWH is positively related to the angle between currents and waves. Statistically, wave height can be underestimated (overestimated) by 4% (3%) on average when the current and waves are in the opposite (same) direction.
2. For swell-dominated cases, the wavenumber spectra between SWH and surface current speed show high similarity with a power law of k^{-2} – k^{-3} at scales of 20–200 km. Moreover, the local wave height gradient is positively related to current vorticity.
3. By averaging along-track wave data over 45 mesoscale eddies, it is found that the SWH and wavelength inside warm (cold) eddies are higher (lower) than those outside the eddies by approximately 5% and 8% (4% and 4%), respectively. In terms of direction, waves are deflected by 11° anticlockwise (11° clockwise) by warm (cold) eddies.
4. Convergence and divergence of waves, which could result in variation in SWH of >0.4 m owing to refraction, can be captured by altimeter-derived wave height. The curvature of wave rays can lead to a change in wave direction of more than 40° when propagating approximately 200 km.
5. Stokes drift is shown to account for 54% of reanalysis current, i.e., contribute markedly to the sea surface current. By considering Stokes drift calculated using the directional spectrum the estimated sea surface currents could be improved by 4% on average and up to 14%.

In this study, we investigate the surface wave variations in the background current field of the KE region based on measurements from both drift buoys and CFOSAT, which has greatly enriched the understanding of wave-current interactions in this region. However, it is still impossible to fully separate the various mechanisms, just like control run numerical experiments, from the presented observations even sometimes we only focus on the cases with relative ideal environmental conditions. Another limitation is that the reanalysis data used in this study, e.g., the sea surface current data, lack representation of the wave-current coupling effect, which introduces uncertainties in quantifying the responses of both waves and currents resulting from their interactions. To improve on this, use of a fully coupled air-ocean-wave model with reliable parameterizations and joint observations of winds, currents, and waves will be of paramount importance.

Acknowledgements We thank the crew of the R/V Dongfanghong 3, as well as the technicians in Qingdao Haiyan Electronics Co. Ltd for their great supports.

Author contributions Methodology: H. W. and J. L.; Formal analysis and investigation: H. W. and J. L.; Writing - original draft preparation: H. W. and J. L.; Writing - review and editing: J. L., Z. C. and X. M.; Funding acquisition: J. L., Z. C. and X. M.; Resources: H. W., J. L., Z. C. and X. M.

Funding This work was supported by the Fundamental Research Funds for the Central Universities (202262005), National Natural Science Foundation of China (42225601, 42176018) and National Key R&D Program of China (2021YFC***1105).

Data availability The observed data by drifting wave buoys analyzed in this study are publicly available from Figshare repository (<https://doi.org/10.6084/m9.fig-share.14498679>). The CFOSAT data are collected from the Archiving, Validation and Interpretation of Satellite Oceanographic data (<https://www.aviso.altimetry.fr/en/home.html>). All of the reanalyzed data in this paper are downloaded from Copernicus Marine Service (<https://marine.copernicus.eu>).

Declarations

Competing interests The authors declare no competing interests.

References

- Ardhuin F, Roland A, Dumas F, Bennis A-C, Sentchev A, Forget P, Wolf J, Girard F, Osuna P, Benoit M (2012) Numerical Wave modeling in conditions with strong currents: dissipation, refraction, and relative wind. *J Phys Oceanogr* 42(12):2101–2120. <https://doi.org/10.1175/JPO-D-11-0220.1>
- Ardhuin F, Gille ST, Menemenlis D, Rocha CB, Rasclé N, Chapron B, Gula J, Molemaker J (2017) Small-scale open ocean currents have large effects on wind wave heights. *J Geophys Research: Oceans* 122(6):4500–4517. <https://doi.org/10.1002/2016jc012413>
- Breivik Ø, Janssen PAEM, Bidlot J-R (2014) Approximate Stokes Drift Profiles in Deep Water. *J Phys Oceanogr* 44(9):2433–2445. <https://doi.org/10.1175/jpo-d-14-0020.1>
- BÜhler O, McIntyre ME (2005) Wave capture and wave–vortex duality. *J Fluid Mech* 534:67–95. <https://doi.org/10.1017/S0022112005004374>
- Chelton DB, Xie S-P (2010) Coupled ocean–atmosphere interaction at oceanic mesoscales. *Oceanography* 23:52–69. <https://doi.org/10.5670/oceanog.2010.05>
- Cheng T, Chen Z, Li J, Ma X, Wen Q, Wu L (2022) Surface wave height regulated by ocean currents: an observational perspective. *Deep Sea Res Part I* 179:103666. <https://doi.org/10.1016/j.dsr.2021.103666>
- Craik ADD, Leibovich S (1976) A rational model for Langmuir circulations. *J Fluid Mech* 73(3):401–426. <https://doi.org/10.1017/S0022112076001420>
- De Carlo M, Ardhuin F, Ollivier A, Nigou A (2023) Wave groups and small scale variability of Wave Heights observed by Altimeters. *J Geophys Research: Oceans* 128(8):e2023JC019740. <https://doi.org/10.1029/2023JC019740>
- Dysthe KB (2001) Refraction of gravity waves by weak current gradients. *J Fluid Mech* 442:157–159. <https://doi.org/10.1017/S0022112001005237>
- Echevarria ER, Hemer MA, Holbrook NJ (2021) Global implications of surface current modulation of the wind-wave field. *Ocean Model* 161:101792. <https://doi.org/10.1016/j.ocemod.2021.101792>
- Frenger I, Gruber N, Knutti R, Münnich M (2013) Imprint of Southern Ocean eddies on winds, clouds and rainfall. *Nat Geosci* 6(8):608–612. <https://doi.org/10.1038/ngeo1863>
- Hauser D, Tison C, Amiot T, Delaye L, Corcoral N, Castellan P (2017) SWIM: the First Spaceborne Wave Scatterometer. *IEEE Trans Geosci Remote Sens* 55(5):3000–3014. <https://doi.org/10.1109/TGRS.2017.2658672>
- Hauser D, Tourain C, Hermozo L, Alraddawi D, Aouf L, Chapron B, Daphinet A, Delaye L, Dalila M, Dormy E, Gouillon F, Gressani V, Grouazel A, Guitton G, Husson R, Mironov A, Mouche A, Ollivier A, Oruba L, Tran N (2021) New observations from the SWIM Radar On-Board CFOSAT: Instrument Validation and Ocean Wave Measurement Assessment. *IEEE Trans Geosci Remote Sens* 59(1):5–26. <https://doi.org/10.1109/TGRS.2020.2994372>
- Hisaki Y (2023) Use of drifting buoys for wave observation: Effect of current on wave data. *Deep Sea Research Part I: Oceanographic Research Papers*. 195:103986. <https://doi.org/10.1016/j.dsr.2023.103986>
- Hwang PA (2005) Altimeter measurements of wind and Wave Modulation by the Kuroshio in the Yellow and East China seas. *J Oceanogr* 61(5):987–993. <https://doi.org/10.1007/s10872-006-0015-0>
- Irvine DE, Tilley DG (1988) Ocean wave directional spectra and wave-current interaction in the Agulhas from the Shuttle Imaging Radar-B synthetic aperture radar. *J Phys Res* 93(C12):15389–15401. <https://doi.org/10.1029/JC093iC12p15389>
- Kenyon KE (1971) Wave refraction in ocean currents. *Deep Sea Res Oceanogr Abstracts* 18(10):1023–1034. [https://doi.org/10.1016/0011-7471\(71\)90006-4](https://doi.org/10.1016/0011-7471(71)90006-4)
- Komen GJ, Cavaleri L, Donelan M, Hasselmann K, Hasselmann S, Janssen PAEM (1994) Dynamics and Modelling of Ocean Waves. Cambridge University Press, <https://doi.org/10.1017/CBO9780511628955>
- Kudryavtsev V, Yurovskaya M, Chapron B, Collard F, Donlon C (2017) Sun glitter imagery of ocean surface waves. Part 1: directional spectrum retrieval and validation. *J Geophys Research: Oceans* 122(2):1369–1383. <https://doi.org/10.1002/2016jc012425>
- Lavrenov IV (1998) The Wave Energy Concentration at the Agulhas Current off South Africa. *Nat Hazards* 17(2):117–127. <https://doi.org/10.1023/A:1007978326982>

- Li R, Wu K, Li J, Dong X, Sun J, Zhang W, Liu Q (2022) Relating a large-scale variation of waves in the Indian Ocean to the IOD. *J Geophys Research: Oceans* 127(10). <https://doi.org/10.1029/2022jc018941>. e2022JC018941
- Longuet-Higgins MS, Stewart R (1962) Radiation stress and mass transport in gravity waves, with application to 'surf beats'. *J Fluid Mech* 13(4):481–504. <https://doi.org/10.1017/S0022112062000877>
- Marechal G, de Marez C (2021) Variability of wind wave field by realistic mesoscale and submesoscale eddy field. *Ocean Sci Discuss* 53:1–18. <https://doi.org/10.5194/os-2021-53>
- McWilliams JC, Sullivan PP, Moeng C-H (1997) Langmuir turbulence in the ocean. *J Fluid Mech* 334:1–30. <https://doi.org/10.1017/S0022112096004375>
- Melville W, Romero L, Kleiss J, Swift R (2005) Extreme wave events in the Gulf of Tehuantepec. *Rogue Waves: Proc. 14th 'Aha Huliko 'a Hawaiian Winter Workshop, Honolulu, HI: University of Hawaii at Manoa*
- Peregrine DH (1976) Interaction of Water Waves and Currents. In C.-S. Yih (Ed.), *Advances in Applied Mechanics* (Vol. 16, pp. 9–117). Elsevier. [https://doi.org/10.1016/S0065-2156\(08\)70087-5](https://doi.org/10.1016/S0065-2156(08)70087-5)
- Poulain P, Gerin R, Mauri E, Pennel R (2009) Wind effects on Drogued and Undrogued drifters in the Eastern Mediterranean. *J Atmos Ocean Technol* 26(6):1144–1156. <https://doi.org/10.1175/2008JT ECHO618.1>
- Quilfen Y, Chapron B (2019) Ocean Surface Wave-Current signatures from Satellite Altimeter measurements. *Geophys Res Lett* 46(1):253–261. <https://doi.org/10.1029/2018gl081029>
- Quilfen Y, Yurovskaya M, Chapron B, Ardhuin F (2018) Storm waves focusing and steepening in the Agulhas current: Satellite observations and modeling. *Remote Sens Environ* 216:561–571. <https://doi.org/10.1016/j.rse.2018.07.020>
- Romero L, Lenain L, Melville WK (2017) Observations of Surface Wave-Current Interaction. *J Phys Oceanogr* 47(3):615–632. <https://doi.org/10.1175/jpo-d-16-0108.1>
- Romero L, Hypolite D, McWilliams JC (2020) Submesoscale current effects on surface waves. *Ocean Model* 153:101662. <https://doi.org/10.1016/j.ocemod.2020.101662>
- Stokes GG (1847) On the theory of oscillatory waves. *Trans Cam Philos Soc* 8:441–455. <https://cir.nii.ac.jp/crid/1574231874864847872>
- Tamura H, Miyazawa Y, Oey L-Y (2012) The Stokes drift and wave induced-mass flux in the North Pacific. *J Geophys Research: Oceans* 117(C8):C08021. <https://doi.org/10.1029/2012jc008113>
- Tan K, Xie L, Bai P, Zheng Q, Li J, Xu Y, Li M (2023) Modulation effects of Mesoscale eddies on Sea Surface Wave fields in the South China Sea Derived from a Wave Spectrometer Onboard the China-France Ocean Satellite. *J Geophys Research: Oceans* 128(1). <https://doi.org/10.1029/2021jc018088>. e2021JC018088
- Tolman HL (1991) A third-generation model for wind waves on slowly varying, unsteady, and inhomogeneous depths and currents. *J Phys Oceanogr* 21(6):782–797. [https://doi.org/10.1175/1520-0485\(1991\)021%3C0782:ATGMFW%3E2.0.CO;2](https://doi.org/10.1175/1520-0485(1991)021%3C0782:ATGMFW%3E2.0.CO;2)
- van den Bremer TS, Breivik Ø, Mathematical A (2018) *Phys Eng Sci*, 376(2111): 20170104. <https://doi.org/10.1098/rsta.2017.0104>
- Villas Bôas AB, Cornuelle BD, Mazloff MR, Gille ST, Ardhuin F (2020) Wave-current interactions at Meso- and submesoscales: insights from Idealized Numerical simulations. *J Phys Oceanogr* 50(12):3483–3500. <https://doi.org/10.1175/jpo-d-20-0151.1>
- Wang DW, Liu AK, Peng CY, Meindl EA (1994) Wave-current interaction near the Gulf Stream during the Surface Wave Dynamics Experiment. *J Geophys Research: Oceans* 99(C3):5065–5079. <https://doi.org/10.1029/93JC02714>
- Wang J, Dong C, Yu K (2020) The influences of the Kuroshio on wave characteristics and wave energy distribution in the East China Sea. *Deep Sea Research Part I: Oceanographic Research Papers*. 158:103228. <https://doi.org/10.1016/j.dsr.2020.103228>
- Wang J, Bethel BJ, Dong C, Li C, Cao Y (2022) Numerical Simulation and Observational Data Analysis of Mesoscale Eddy effects on Surface waves in the South China Sea. *Remote Sens* 14(6):1463. <https://doi.org/10.3390/rs14061463>
- Webb A, Fox-Kemper B (2015) Impacts of wave spreading and multidirectional waves on estimating Stokes drift. *Ocean Model* 96:49–64. <https://doi.org/10.1016/j.ocemod.2014.12.007>
- Xu Y, Liu J, Xie L, Sun C, Liu J, Li J, Xian D (2019) China-France Oceanography Satellite (CFOSAT) simultaneously observes the typhoon-induced wind and wave fields. *Acta Oceanol Sin* 38(11):158–161. <https://doi.org/10.1007/s13131-019-1506-3>

Publisher's note Springer Nature remains neutral with regard to jurisdictional claims in published maps and institutional affiliations.

Springer Nature or its licensor (e.g. a society or other partner) holds exclusive rights to this article under a publishing agreement with the author(s) or other rightsholder(s); author self-archiving of the accepted manuscript version of this article is solely governed by the terms of such publishing agreement and applicable law.